ACS APPLIED MATERIALS & INTERFACES

Letter

www.acsami.org

Nano-petri-dish Array Assisted Glancing Angle Sputtering for Ag-NP Assembled Bi-nanoring Arrays as Effective SERS Substrates

Xiaoye Hu,[†] Guowen Meng,*[,†,‡] Qing Huang,[§] Chuhong Zhu,[†] Bensong Chen,[†] Zhulin Huang,[†] Fadi Li,[†] and Zhaoming Wang[†]

[†]Key Laboratory of Materials Physics, and Anhui Key Laboratory of Nanomaterials and Nanostructures, Institute of Solid State Physics, Chinese Academy of Sciences, Hefei, Anhui 230031, People's Republic of China

[‡]University of Science and Technology of China, Hefei 230026, People's Republic of China

[§]Key Laboratory of Ion Beam Bioengineering, Institute of Technical Biology & Agriculture Engineering, Hefei Institutes of Physical Sciences, Chinese Academy of Sciences, Hefei 230031, People's Republic of China

Supporting Information

ABSTRACT: Nano-petri-dish array assisted glancing angle Ag-sputtering was reported to synthesize Ag-nanoparticle (Ag-NP) assembled bi-nanoring arrays as surface-enhanced Raman scattering (SERS) substrates. By manipulating the sputtering-Ag duration, the gaps between the Ag-NPs in the bi-nanorings are tunable to acquire optimal electromagnetic field enhancement, and the ordered bi-nanoring arrays ensure excellent reproducibility for Raman measurement. Such as-fabricated Ag-NPs assembled nanoring arrays exhibit excellent SERS performance, not only 1×10^{-12} M rhodamine 6G has been identified, but also polychlorinated biphenyls with a low concentration down to 1×10^{-9} M has been recognized, showing great potential in the detection of trace organic pollutants in the environment.

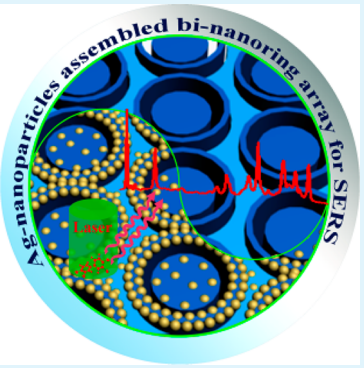

KEYWORDS: *surface-enhanced Raman scattering, localized surface plasmon resonance, Ag-nanoparticle assembly, bi-nanoring array*

1. INTRODUCTION

Noble metallic nanostructures have been intensively explored for sensitive detection of molecules owing to their extremely high electromagnetic field enhancement resulting from localized surface plasmon resonance (LSPR).[1−4] For example, there is an LSPR-induced surface-enhanced Raman scattering (SERS) effect,[5,6] which can make the Raman signals of the target molecules adsorbed on the noble metallic nanostructures enhanced by several orders of magnitude higher. Nowadays SERS-based ultrasensitive detection of some chemicals has been achieved.[7−11] It is generally acknowledged that enormous SERS effect is mainly located at the so-called plasmonic "hot spots", for example, the sub-10 nm gaps between the adjacent nano-building-blocks of the SERS substrate.[12−17] Therefore, one pursuit for SERS-based detection is to fabricate noble metallic nanostructures with controllable plasmonic hot spots. As colloids of Ag/Au nanoparticles (NPs) are relatively easy to synthesize and form sub-10 nm gaps within their aggregates, they are widely adopted for SERS application, and giant enhancement factor up to $\sim 1 \times 10^{14}$ has been achieved.[14,15] However, in such a system of Ag/Au-NPs colloids, the hot spots are randomly distributed, so it is hard to acquire reproducible SERS signals.[18,19] To overcome this shortcoming, regularly ordered noble metallic nanostructures attract more attention, because they possess nano-building-blocks in a uniform distribution fashion over large areas and thus give rise to better Raman signal reproducibility. Therefore, much effort has recently been devoted to the fabrication of regularly-arranged noble metallic nanostructures as SERS-substrates, such as aligned arrays of nanodisks[20] via electron beam lithography, arrays of nanorods[21] or nanowires[22−24] via a porous anodized alumina template-assisted approach, and highly ordered periodic two-dimensional close-packed noble metal nanoparticles or films via polystyrene sphere template-assisted approach.[25−27] Nevertheless, it is still a great challenge to acquire regularly-arranged noble metallic nanostructures with high SERS-activity. One obstacle is that this normally requires complex and precise manipulation techniques[28] or special treatment processes[22] to reduce the gaps between the neighboring nano-building-blocks to the sub-10 nm range so that enough hot spots are produced.

To achieve nano-building-block assembled regularly arranged noble metallic nanostructure arrays with both high SERS activity and signal reproducibility, we herein present a nanoscale petri-dish array template assisted glancing angle deposition approach to the ordered arrays of Ag-nanoparticles (Ag-NPs) assembled concentric bi-nanorings as effective SERS-substrates, as shown schematically in Scheme 1. Firstly, ordered

Received: February 17, 2014
Accepted: May 28, 2014
Published: May 28, 2014

   dx.doi.org/10.1021/am502793d | ACS Appl. Mater. Interfaces 2014, 6, 7991−7995

Scheme 1. Schematic for the Fabrication of Ag-NP Assembled Bi-nanoring Arrays: (a) Anodic TiO_2−NT Arrays, (b) TiO_2-Nano-petri-dish Array Template, (c) Ag-NP Assembled Concentric Bi-nanoring Arrays; Lower-Right Panel Is a Schematic for One Cycle of Glancing Angle Sputtering, Where Ag-Spheres with a Given Color Are Sputtered onto the Outer and Inner of the Petri-Dish Brim for Each Direction Sputtering, As Shown by One of the Enlarged Petri-dishes Assembled with Ag-NPs in the Middle

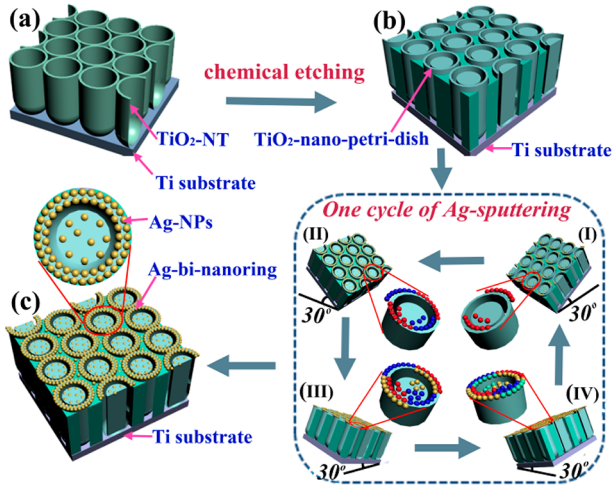

anodic TiO_2 nanotube (NT) arrays are grown on Ti-foil (Scheme 1a) by a two-step anodization of Ti-foil.[29] Then, by controlled wet chemical etching the anodic TiO_2−NT arrays in KOH and HCl solutions sequentially, each TiO_2−NT is in situ converted into a nanoscale petri-dish-like structure (denoted as nano-petri-dish), forming regularly arranged TiO_2-nano-petri-dish arrays (Scheme 1b). Next, by glancing angle Ag-sputtering from four different directions sequentially (See the lower-right of Scheme 1), Ag-NPs are assembled around the outer and inner of the brim of each nano-petri-dish, forming ordered arrays of Ag-NPs assembled concentric bi-nanorings around each of the nano-petri-dishes (Scheme 1c) (Experimental details can be found in Part S1 in the Supporting Information). The resultant Ag-NPs assembled concentric bi-nanoring arrays have the following advantages. On one hand, the large-area highly ordered arrays of Ag-NPs assembled concentric bi-nanorings can give rise to the good reproducibility of the Raman signals throughout the whole substrates. On the other hand, the facile manipulation of the Ag-NPs in the bi-nanorings makes it easy to tune the gaps between the neighboring Ag-NPs in the same concentric bi-nanoring and those between the two adjacent nanorings to sub-10 nm range, thus the electromagnetic field enhancement and the SERS-activity can be optimized. As a result, the Ag-NPs assembled concentric bi-nanoring arrays display remarkable SERS sensitivity and signal reproducibility. Using our Ag-NPs assembled concentric bi-nanoring arrays as SERS-substrates, not only rhodamine 6G (R6G) with a concentration down to 1×10^{-12} M has been identified, but also PCB-77 (one congener of polychlorinated biphenyls, a notorious class of persistent organic pollutants) with a low concentration down to 1×10^{-9} M has been recognized, showing great potential in detection of trace organic pollutants in the environment.

2. RESULTS AND DISCUSSION

After the two-step anodization of pure Ti foil,[29] top-view scanning electron microscope (SEM) observation (Figure 1a) reveals the close-packed hexagonally ordered anodic TiO_2−NTs arrays over a large area on the remaining Ti foil. After chemical etching the anodic TiO_2−NT arrays in KOH and HCl solutions sequentially, TiO_2 nano-petri-dish arrays are obtained, as shown in Figure 1b−d. It can be observed that different from the close-packed arrangement of the TiO_2−NTs, the TiO_2-nano-petri-dishes are independent of each other, leaving gaps with several-dozens nanometers. For clarity, a schematic of the nano-petri-dishes are shown in the inset of Figure 1b. Moreover, an oblique-view (Figure 1d) at 15° reveals that the brim of the TiO_2-nano-petri-dish is about 30 nm high. As for the formation mechanism of TiO_2-nano-petri-dish, we prelimi-

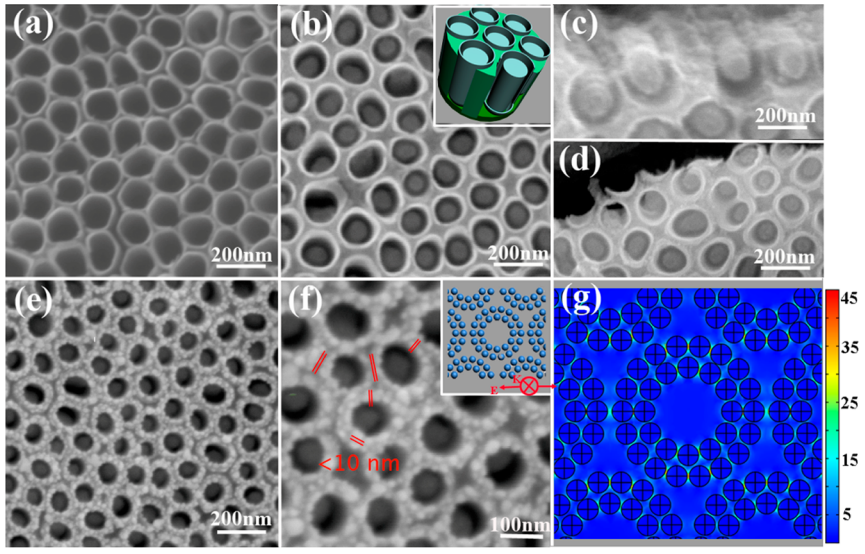

Figure 1. (a−d) SEM images of (a) the TiO_2−NT arrays and the TiO_2-nano-petri-dish arrays from (b) top-, (c) cross-sectional, and (d) oblique-view, respectively. The inset in b is a schematic of a small part of the TiO_2-nano-petri-dish arrays. (e, f) SEM images of the Ag-NP assembled concentric bi-nanoring arrays, (f) the enlarged view shows some sub-10 nm gaps between the neighboring Ag-NPs marked with red. The inset in f is a schematic for one of the concentric bi-nanorings. (g) E-field intensity distribution in one of the Ag-NP assembled concentric bi-nanoring arrays.

dx.doi.org/10.1021/am502793d | ACS Appl. Mater. Interfaces 2014, 6, 7991−7995

narily suggest that a dissolution-coagulation process of TiO_2−NTs in KOH and HCl solutions can in situ convert each TiO_2−NT into a TiO_2-nano-petri-dish structure (see Part S2 and Figure S1 in the Supporting Information), being similar to the s relevant reports.[30,31]

Next, glancing angle Ag-sputtering was performed on the TiO_2-nano-petri-dish array template inclined at an oblique angle of 30° on the objective table. Glancing angle Ag-sputtering can ensure Ag-NPs to deposit on both the inner and the outer of the brim of the nano-petri-dish. To achieve Ag-NP assembled bi-nanoring morphology, Ag-sputtering was carried out from four different directions for two cycles (Steps I to IV for one cycle shown schematically in the lower-right panel of Scheme 1), with each direction taking the same sputtering duration. The Ag-sputtering of two cycles can effectively split the Ag-sputtering duration in the same direction, avoiding the aggregation of Ag-NPs resulting from the long time continuously Ag-sputtering in the same direction (Part S3 and Figure S2 in the Supporting Information), thus forming disperse Ag-NPs on both the inner and the outer of the brim of the nano-petri-dish. Moreover, the size of the Ag-NPs as well as the adjacent gaps between the Ag-NPs can be manipulated by tuning the Ag-sputtering duration of each direction. Figure 1e shows the morphologies of the representative Ag-NPs assembled concentric bi-nanoring arrays achieved with Ag-sputtering for 10 min. The enlarged view (Figure 1f) indicates that Ag-NPs with sub-10 nm adjacent gaps are sputtered onto the inner and outer of the brim of the TiO_2-nano-petri-dishes, forming Ag-NPs assembled concentric bi-nanoring arrays (schematic of one bi-nanoring is shown in the Inset of Figure 1f). For such concentric bi-nanoring arrays, the LSPR is generated within the gaps (<10 nm) between the adjacent Ag-NPs assembled in the same concentric bi-nanorings and between some neighboring nanorings, as confirmed by finite-element method (FEM) modeling (Figure 1g, detailed method of FEM modeling can be seen in Part S4 of Supporting Information). In contrast, the gaps existing in the same concentric bi-nanorings hold great majority, and primarily drive the LSPR. To further elucidate the gap-induced LSPR between the adjacent Ag-NPs, we also used FEM modeling to investigate the localized electric field intensity of the Ag-NPs assembled concentric bi-nanorings with varied Ag-NP sizes and gaps (Figure 2). It can be seen that the localized electric field intensity is enhanced with the increase of the Ag-NP size within diameter of about 25 nm range (Figure 2a−c) and the abridgement of the inter-NP gaps. As the Ag-NP diameters are increased to or beyond about 25 nm with the increase of Ag-sputtering duration, the adjacent Ag-NPs in the same nanoring interconnect to form a coarse nanoring, giving rise to the disappearance of inter-NP gaps, thus the enhancement of the localized electric field intensity reduces (Figure 2d). However, with further elongation of the Ag-sputtering duration, the Ag-NPs on the outer and inner brim of the TiO_2-nano-petri-dishs are overlapped in axial direction to form coarse nanorings with a certain height. Moreover, many gaps between the two neighboring coarse nanorings can also be abridged to or kept within sub-10 nm range, generating hot spots within these gaps between the neighboring coarse nanorings, and thus resulting in the enhancement of the LSPR again, which was confirmed in both our experiments and FEM simulations as follows. For example, when the Ag-sputtering duration is elongated to 16 min, many sub-10 nm gaps appear in between the two neighboring coarse nanorings (see Part S5 and Figure S5 in the

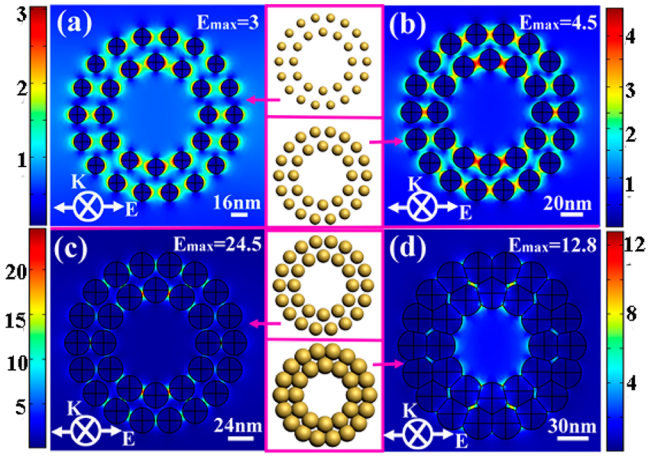

Figure 2. Localized electric field intensity and distribution for the Ag-NPs assembled concentric bi-nanorings with the NPs having various diameters, (a) 16, (b) 20, (c) 24, and (d) 30 nm.

Supporting Information). The FEM modeling result displays the evident enhancement of LSPR within the gaps between the neighboring coarse nanorings. Obviously, if the Ag-sputtering duration is further elongated, the adjacent gaps between the two neighboring coarse nanorings will disappear, and finally the LSPR of substrate will be weakened. It should be noted that, for the actual situation in our experiments, the distribution and size of the Ag-NPs formed the concentric bi-nanoring might be not so uniform as the ideal model. To more accurately reflect the varieties of the LSPR with the size of the Ng-NPs, therefore, we also established the more realistic model structures for the FEM simulations (See Part S6 and Figure S6 in the Supporting Information). The results indicate that the variation trend of the localized electric field intensities with the size of the Ag-NPs is consistent with that of the ideal models.

To further show the tunability for the localized electric field intensity of the Ag-NPs assembled nanorings via manipulating the Ag-sputtering duration, as well as to obtain the substrate with optimal SERS effect, we tested the SERS activities of various Ag- assembled nanoring arrays with different Ag-sputtering durations by using R6G as the standard target analyte while maintaining other measurement conditions the same. Figure 3a displays the SERS spectra of 1×10^{-8} M R6G adsorbed on the as-fabricated substrates with varied Ag-sputtering durations. The trend of variety for the SERS activity can be intuitively described by comparing the intensities of Raman peaks at 614 cm^{-1} by drawing the bar charts (Figure 3b) with the plot's ordinate and abscissa describing the Raman intensity and the Ag-sputtering duration, respectively. It can be seen that the peak intensities increase with Ag-sputtering for the first 10 min, corresponding to the increase of the Ag-NP size and the abridgement of inter-NP gap. When the Ag-sputtering duration is about 10 min, most intergaps between the adjacent Ag-NPs are less than 10 nm (as shown in Figure 1f), and the peak intensities reach the peak values. Then, the peak intensities reduce with the elongation of Ag-sputtering duration, resulting from the disappearance of inter-NP gap. Nevertheless, with further elongation of Ag-sputtering duration, the formation of the Ag-NPs assembled coarse nanorings and the generation of sub-10 nm gaps between the two neighboring coarse nanorings result in the enhancement of peak intensities again. Finally, with Ag-sputtering goes on the gaps between the

dx.doi.org/10.1021/am502793d | ACS Appl. Mater. Interfaces 2014, 6, 7991−7995

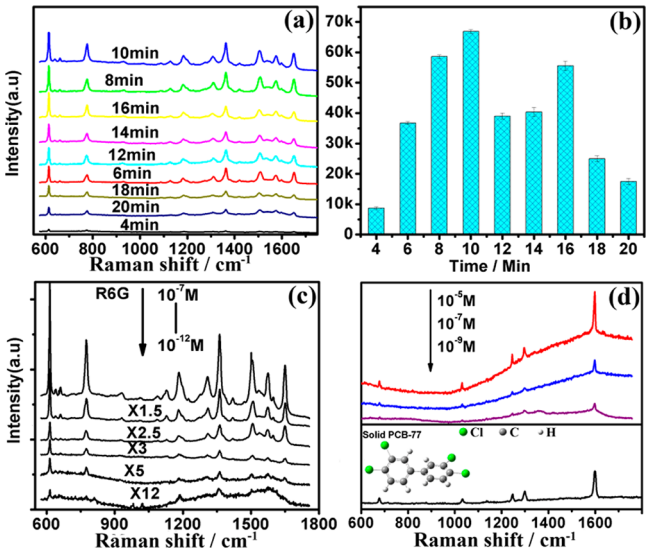

Figure 3. (a) SERS spectra of 1×10^{-8} M R6G adsorbed on the Ag-NPs assembled nanoring arrays with different Ag-sputtering durations, the integration time was 10 s. (b) Bar chart for the changes of the intensities of Raman peaks at 614 cm^{-1} with different Ag-sputtering durations. (c) Raman spectra of R6G with varied concentrations adsorbed on the Ag-NPs assembled bi-nanoring arrays with Ag-sputtering duration of 10 min. (d) Raman spectrum of solid PCB-77 (bottom), and SERS spectra of PCB-77 with different concentrations absorbed on the Ag-NPs assembled concentric bi-nanoring arrays. The integration time was 20 s.

two neighboring coarse nanorings disappear gradually, thus leading to the decrease in the peak intensities.

Evidently, the Ag-NP assembled bi-nanoring arrays obtained with Ag-sputtering for 10 min exhibit the higher SERS activity than all others Ag-NP assembled nanoring arrays. Moreover, the bi-nanoring arrays also display more excellent SERS activity than the Ag-NP aggregated on the top of anodic TiO_2−NT arrays (see Part S7 and Figure S7 in the Supporting Information). Consequently, the Ag-NPs assembled bi-nanoring arrays with optimal SERS activities were chosen as SERS substrates to check the SERS signal sensitivity and the reproducibility using R6G as probe molecules. Figure 3c shows the Raman spectra of R6G with varied concentrations (1×10^{-7}, 1×10^{-8}, 1×10^{-9}, 1×10^{-10}, 1×10^{-11}, and 1×10^{-12} M) adsorbed on the Ag-NPs assembled bi-nanoring arrays, displaying high-quality SERS signals and low signal/noise ratios. Even when the R6G solution is diluted to 1×10^{-12} M, the characteristic bands of R6G are still clearly visible. The estimation of the average enhancement factors (EF) reveals that the Ag-NP assembled bi-nanoring array has an enhancement of about 1.3×10^8 to 4-ATP at 1077 cm^{-1} (see Part S8 and Figure S8 in the Supporting Information). Additionally, the reproducibility of SERS signal was also checked by examining 21 random spots across the whole substrate using 1×10^{-7} M R6G under the same the laser power and the integration time. The results show good reproducibility as the deviation of band intensity of R6G is less than 10% compared to the average relative peak intensity (see Part S9 and Figure S9 in the Supporting Information). Meanwhile, this good reproducibility of the SERS substrate has also been proven by our Raman mapping measurement (see Part S9 and Figure S10 in the Supporting Information).

To demonstrate the potential practical application of the Ag-NP assembled bi-nanoring arrays with optimized SERS activity, i.e., the Ag-NP assembled bi-nanoring arrays with Ag-sputtering duration of 10 min, we have tried laboratorial detection of trace polychlorinated biphenyls (PCBs, a class of highly toxic persistent organic pollutants that have been found detrimental to human health),[32] as in previous reports.[33,34] As an example, 3,3′,4,4′-pentachlorobiphenyl (PCB-77, one congener of PCBs with its molecular structure shown in Figure 3d) was measured as the trial analyte. Because of the apolar nature, PCBs can be hardly dissolved in water, so various amounts of PCB-77 were dissolved in acetone, and then dispersed on the optimal SERS substrates for measurement. The upper curves in Figure 3d show the SERS spectra of PCB-77 with different concentrations (1×10^{-5}, 1×10^{-7}, and 1×10^{-9} M). It can be seen that five distinct bands at 674 cm^{-1} (C−Cl stretching), 1032 cm^{-1} (ring breathing), 1245 cm^{-1} (C−H wagging), 1295 cm^{-1} (biphenyl C−C bridge stretching), and 1596 cm^{-1} (ring stretching) in the SERS spectra, being corresponding well with those found in the standard Raman spectrum of solid PCB-77 at the bottom of Figure 3d. It also shows that PCB-77 at low concentration down to 1×10^{-9} M can still be identified, and the crucial characteristic bands corresponding to the PCB-77 are distinguishable, suggesting that the optimal Ag-NP assembled bi-nanoring arrays can be used as effective SERS substrates for detection of trace-level PCBs.

3. CONCLUSIONS

In conclusion, we have demonstrated a simple nano-petri-dish array assisted glancing angle Ag-sputtering for the fabrication of Ag-NPs assembled nanoring arrays as effective SERS substrates. By tuning the Ag-sputtering duration, Ag-NP assembled bi-nanorings and coarse nanorings can be obtained, meanwhile the size of Ag-NPs and the gaps between the neighboring Ag-NPs in the same nanoring as well as the gaps between the adjacent nanorings can be tuned, so that the manipulation of the localized electric field intensity and optimization of the SERS activity have been achieved. Such Ag-NP assembled nanoring arrays exhibit both excellent SERS activity and signal reproducibility, and can thus be employed as SERS-based sensors for rapid detection of trace organic pollutants such as PCBs in the environment. As an example, the as-fabricated optimal SERS substrate has been demonstrated to detect the highly stable and volatile PCB-77 with concentration as low as 1×10^{-9} M.

■ ASSOCIATED CONTENT

Ⓢ Supporting Information

Experimental method, formation mechanism of TiO_2-nano-petri-dish arrays, detailed simulation method of the localized electric field intensity via FEM modeling, morphology of coarse nanoring arrays, estimation of enhancement factor, and SERS signal reproducibility of Ag-nanoring arrays. This material is available free of charge via Internet at http://pubs.acs.org.

■ AUTHOR INFORMATION

Corresponding Author

*E-mail: gwmeng@issp.ac.cn.

Notes

The authors declare no competing financial interest.

■ ACKNOWLEDGMENTS

This work was supported by the National Basic Research Program of China (Grant 2013CB934304), and the NSFC (Grants 51101151, 11274312, and 11175204).

■ REFERENCES

(1) Bolduc, O. R.; Masson, J. F. Advances in Surface Plasmon Resonance Sensing with Nanoparticles and Thin Films: Nanomaterials, Surface Chemistry, and Hybrid Plasmonic Techniques. *Anal. Chem.* **2011**, *83*, 8057−8062.

(2) Shen, Y.; Zhou, J. H.; Liu, T. R.; Tao, T. T.; Jiang, R. B.; Liu, M. X.; Xiao, G. H.; Zhu, J. H.; Zhou, Z. K.; Wang, X. H.; Jin, C. J.; Wang, J. F. Plasmonic Gold Mushroon Arrays with Refractive Index Sensing Figures of Merit Approaching The Theoretical Limit. *Nat. Commun.* **2013**, *4*, 1−9.

(3) Kabashin, A. V.; Evans, P.; Pastovsky, S.; Hendren, W.; Wurtz, G. A.; Pollard, R.; Podolskiy, V. A.; Zayats, A. V. Plasmonic Nanorod Metamaterials for Biosensing. *Nat. Mater.* **2009**, *8*, 867−871.

(4) Lee, K.; Jang, D. H.; Lee, K. S.; Kim, W. M.; Sohn, Y. S. Enhancing Performance of a Miniaturized Surface Plasmon Resonance Sensor in The Reflectance Detection Mode Using a Waveguide-Coupled Bimetallic Chip. *Nano. Res. Lett.* **2013**, *8*, 344−352.

(5) Li, J. F.; Huang, Y. F.; Ding, Y.; Yang, Z. L.; Li, S. B.; Zhou, X. S.; Fu, F. R.; Zhang, W.; Zhou, Z. Y.; Wu, D.; Tian, Z. Q. Shell-Isolated Nanoparticle Enhanced Raman Spectroscopy. *Nature* **2010**, *464*, 392−395.

(6) Smythe, E. J.; Dickey, M. D.; Bao, J. M.; Whitesides, G. M.; Capasso, F. Optical Antenna Arrays on a Fiber Facet for in situ Surface-Enhanced Raman Scattering Detection. *Nano Lett.* **2009**, *9*, 1132−11.

(7) Lim, D.-K.; Jeon, K.-S.; Kim, H. M.; Nam, J.-M.; Suh, Y. D. Nanogap-engineerable Raman-active Nanodumbbells for Single-Molecue Detection. *Nat. Mater.* **2010**, *9*, 60−67.

(8) Majumdar, D.; Singha, A.; Mondal, P. K.; Kundu, S. DNA-Mediated Wirelike Clusters of Silver Nanoparticles: An Ultrasensitive SERS Substrate. *ACS Appl. Mater. Interfaces.* **2013**, *5*, 7798−7807.

(9) Stranahan, S. M.; Willets, K. A. Super-Resolution Optical Imaging of Single-molecule SERS Hot Spots. *Nano Lett.* **2010**, *10*, 3777−3784.

(10) Kneipp, K.; Wang, Y.; Kneipp, H.; Perelman, L. T.; Itzkan, I.; Dasari, R. R.; Feld, M. S. Single Molecule Detection Using Surface-Enhanced Raman Scattering (SERS). *Phys. Rev. Lett.* **1997**, *78*, 1667−1670.

(11) Xu, H. X.; Bjerneld, E. J.; Käll, M.; Börjesson, L. Spectroscopy of Single Hemoglobin Molecules by Surface Enhanced Raman Scattering. *Phys. Rev. Lett.* **1999**, *83*, 4357−4360.

(12) Zhang, Z.; Wen, Y.; Ma, Y.; Li, J.; Jiang, L.; Song, Y. Mixed DNA-Functionalized Nanoparticle Probes for Surface-Enhanced Raman Scattering-Based Multiplex DNA Detection. *Chem. Commun.* **2011**, *47*, 7407−7409.

(13) Nie, S.; Emory, S. R. Probing Single Molecules and Single Nanoparticles by Surface by Surface-Enhanced Raman Scattering. *Science* **1997**, *275*, 1102−1106.

(14) Wang, Z. J.; Pan, S. L.; Krauss, T. D.; Du, H.; Rothberg, L. J. The Structural Basis for Giant Enhancement Enabling Single-Molecule Raman Scattering. *Proc. Natl. Acad. Sci. U.S.A.* **2003**, *100*, 8638−8643.

(15) Michaels, A. M.; Nirmal, M.; Brus, L. E. Surface Enhanced Raman Spectroscopy of Individual Rhodamine 6G Molecules on Large Ag Nanocrystals. *J. Am. Chem. Soc.* **1999**, *121*, 9932−9939.

(16) Tang, H.; Meng, G.; Huang, Q.; Zhang, Z.; Huang, Z.; Zhu, C. Arrays of Cone-Shaped ZnO Nanorods Decorated with Ag Nanoparticles as 3D Surface-Enhanced Raman Scattering Substrates for Rapid Detection of Trace Polychlorinated Biphenyls. *Adv. Funct. Mater.* **2012**, *1*, 218−224.

(17) Zhu, C.; Meng, G.; Huang, Q.; Zhang, Z.; Xu, Q.; Liu, G.; Huang, Z.; Chu, Z. Ag Nanosheet-Assembled Micro-Hemispheres as Effective SERS Substrates. *Chem. Commun.* **2011**, *47*, 2709−2711.

(18) Li, W. Y.; Camargo, P. H. C.; Lu, X. M.; Xia, Y. N. Dimers of Silver Nanospheres: Facile Synthesis and Their Use as Hot Spots for Surface-Enhanced Raman Scattering. *Nano Lett.* **2009**, *9*, 485−490.

(19) Laurence, T. A.; Braun, G.; Talley, C.; Schwartzberg, A.; Moskovits, M.; Reich, N.; Huser, T. R. Solution-Based Characterization of Optimized SERS Nanoparticle Substrates. *J. Am. Chem. Soc.* **2009**, *131*, 162−169.

(20) Yu, Q.; Guan, P.; Qin, D.; Golden, G.; Wallace, P. M. Inverted Size-Dependence of Surface-Enhanced Raman Scattering on Gold Nanohole and Nanodisk Arrays. *Nano Lett.* **2008**, *8*, 1923−1928.

(21) Zhou, Q.; Li, Z. C.; Yang, Y.; Zhang, Z. J. Arrays of Aligned, Single Crystalline Silver Nanorods for Trace Amount Detedtion. *J. Phys. D: Appl. Phys.* **2008**, *42*, 152007.

(22) Huang, Z. L.; Meng, G. W.; Huang, Q.; Yang, Y. J.; Zhu, C. H.; Tang, C. L. Improved SERS Performance from Au Nanopillar Arrays by Abridging The Pillar Tip Spacing by Ag Sputtering. *Adv. Mater.* **2010**, *22*, 4136−4139.

(23) Lee, S. J.; Morrill, A. R.; Moskovits, M. Hot Spots in Silver Nanowire Bundles for Surface-Enhanced Raman Spectroscopy. *J. Am. Chem. Soc.* **2006**, *128*, 2200−2201.

(24) Jeong, D. H.; Zhang, Y. X.; Moskovits, M. Polarized Surface Enhanced Raman Scattering from Aligned Silver Nanowire Rafts. *J. Phys. Chem. B* **2004**, *108*, 12724−12728.

(25) Tian, C.; Liu, Z.; Jin, J.; Lebedkin, S.; Huang, C.; You, H.; Liu, R.; Wang, L.; Song, X.; Ding, B.; Walheim, S.; Schimmel, T.; Fang, J. Gold Mesoflower Arrays with Sub-10 nm Intraparticle Gaps for Highly Sensitive and Repeatable Surface Enhanced Raman Spectroscopy. *Nanotechnology* **2012**, *23*, 165604.

(26) Šloufova-Srnova, I.; Vlčková, B. Two-dimensional Assembling of Au Nanoparticles Mediated by Tetrapyridylporphine Molecules. *Nano Lett.* **2002**, *2*, 121−125.

(27) Yang, S. K.; Cai, W. P.; Kong, L. C.; Lei, Y. Surface Nanometer-Scale Patterning in Realizing Large-Scale Ordered Arrays of Metallic Nanoshells with Well-Defined Structures and Controllable Properties. *Adv. Funct. Mater.* **2010**, *20*, 2527−2533.

(28) Huang, Z. L.; Meng, G. W.; Huang, Q.; Chen, B.; Zhu, C.; Zhang, Z. Large-Area Ag Nanorod Array Substrates for SERS: AAO Template-Assisted Fabrication Functionalization, and Application in Detection PCBs. *J. Raman. Spectrosc.* **2013**, *44*, 240−246.

(29) Zhang, T. C.; Hu, X. Y.; Fang, M.; Zhang, L. D.; Wang, Z. M. Synthesis of Hierarchical TiO_2 Nanotube Arrays Assembled by Anatase Single Crystal Nanoparticles. *CrystEngComm.* **2012**, *1*, 7656−7661.

(30) Bavykin, D. V.; Friedrich, J. M.; Walsh, F. C. Protonated Titanates and TiO_2 Nanostructured Materials: Synthesis, Properties, and Applications. *Adv. Mater.* **2006**, *18*, 2087−2824.

(31) Sun, X. M.; Li, Y. D. Sythesis and Characterization of Ion-Exchangeable Titanate Nanotubes. *Chem.—Eur. J.* **2003**, *9*, 2229−2238.

(32) Ross, G. The Public Health Implications of Polychlorinated Phenyls (PCBs) in The Environment. *Ecotoxicol. Environ. Saf.* **2004**, *59*, 275−291.

(33) Bantz, K. C.; Haynes, C. L. Surface-enhanced Raman Scattering Detection and Discrimination of Polychlorinated Biphenyls. *Vib. Spectrosc.* **2009**, *50*, 29−35.

(34) Zhou, Q.; Yang, Y.; Ni, J.; Li, Z.; Zhang, Z. Rapid Recognition of Isomers of Monochlorobiphenyls at Trace Levels by Surface-Enhanced Raman Scattering Using Ag Nanorods as a Substrate. *Nano Res.* **2010**, *3*, 423−428.